RSC Advances

ROYAL SOCIETY OF CHEMISTRY

PAPER

View Article Online
View Journal | View Issue

Cite this: *RSC Adv.*, 2021, **11**, 5993

A highly sensitive ppb-level H_2S gas sensor based on fluorophenoxy-substituted phthalocyanine cobalt/rGO hybrids at room temperature†

Bin Wang, *[a] Xiaolin Wang,[b] ZhiJiang Guo,[a] Shijie Gai,[a] Yong Li[a] and Yiqun Wu[ac]

The peripheral and non-peripheral substitution of 4-trifluoromethylphenoxy groups in the design of gas sensing phthalocyanine cobalt/reduced graphene oxide (rGO) hybrids with two different positions of the substituents was realized. Tetra-α(β)-(4-trifluoromethylphenoxy)phthalocyanine cobalt/reduced graphene oxide (3(4)-cF_3poPcCo/rGO) hybrids were prepared through noncovalent interaction, and were analyzed by FT-IR, UV-vis, TGA and SEM. The gas sensing performance of the cF_3poPcCo/rGO hybrid gas sensors towards ppb hydrogen sulfide (H_2S) was measured at room temperature. The results show that the 4-cF_3poPcCo/rGO sensor has better sensitivity, selectivity and reproducibility than the 3-cF_3poPcCo/rGO sensor, as well as a perfect linear response to the concentration of H_2S. For the 4-cF_3poPcCo/rGO sensor, the response sensitivity to 1 ppm H_2S is as high as 46.58, the response and recovery times are 600 s and 50 s for 1 ppm H_2S, and the detection limit is as low as 11.6 ppb. This is mainly due to the loose and porous structure of the cF_3poPcCo/rGO hybrids, the fact that graphene is an excellent conductive agent, and the fact that the electron-withdrawing capability of the trifluoromethyl group can increase the holes of rGO and PcCo. In addition, through electrochemical impedance spectroscopy (EIS) and *I–V* curves, and density functional theory, the influence of different positions of the substituents of cF_3poPcCo/rGO on the sensing performance and the sensing mechanism for improving sensitivity were discussed and confirmed in detail.

Received 16th October 2020
Accepted 12th January 2021

DOI: 10.1039/d0ra08832c

rsc.li/rsc-advances

1. Introduction

In recent years, with the rapid development of the economy and society, people's demand for various resources in life has also increased. This leads to more and more serious environmental damage and pollution, especially air pollution. Among the common air pollutants, hydrogen sulfide (H_2S) is a highly toxic, dangerous and flammable gas with the smell of rotten eggs. H_2S is widely produced in the process of biodegradation in the petroleum industry, natural gas, food, organic materials and bacterial decomposition of human and animal feces.[1–4] According to the safety standards established by the American Conference of governmental industrial hygienists, the threshold value of H_2S is about 10 ppm.[5] In fact, many studies have shown that H_2S higher than 2–5 ppm will have adverse effects on the human respiratory system.[6] Therefore, it is very important to realize the real-time monitoring and effective and accurate detection of the harmful H_2S gas at lower concentrations (such as ppb level).

Recently, many researchers have been devoted to the research and development of new hydrogen sulfide gas sensors based on high selectivity, high sensitivity, high efficiency, energy saving and low detection limit. The use of CuO, WO_3, ZnO, SnO_2, Fe_2O_3 and other metal oxides has been reported to detect H_2S at the ppm level.[7–17] The detection limit of most materials is very low, but the optimal working temperature (OWT) is still very high and the sensitivity is very low. For example, in 2016, the α-Fe_2O_3 sensor prepared by Lin *et al.* had a sensitivity of 11.7 for hydrogen sulfide at 350 °C and 100 ppm.[18] The sensitivity of the α-Fe_2O_3 sensor decorated with titanium dioxide developed by Kheel *et al.*[19] to hydrogen sulfide at 200 ppm was only 7.4 at 300 °C. In 2018, p-type Co_3O_4 prepared by Quang *et al.* exhibited a sensitivity of only 4.5 for the detection of 100 ppm hydrogen sulfide gas at 300 °C.[20] All of the above results confirm that a great breakthrough has been made in the detection of hydrogen sulfide, but it is still a challenge to develop a sensor material for detecting ppb level H_2S with high sensitivity at low temperatures.

Graphene based carbon material, as a two-dimensional carbon material, has also made a great breakthrough in the

[a]*Key Laboratory of Functional Inorganic Material Chemistry, Ministry of Education, School of Chemistry and Materials Science, Heilongjiang University, Harbin 150080, P. R. China. E-mail: wangbin@hlju.edu.cn; Fax: +86 451 86673647; Tel: +86 451 86609121*

[b]*School of Material and Chemical Engineering, Heilongjiang Institute of Technology, Harbin 150050, P. R. China*

[c]*Shanghai Institute of Optics and Fine Mechanics, Chinese Academy of Sciences, Shanghai 201800, P. R. China*

† Electronic supplementary information (ESI) available. See DOI: 10.1039/d0ra08832c

field of hydrogen sulfide gas sensing. For example, in 2014, Seon-Jin Choi *et al.* reported that the reduced graphene oxide-functionalized tin dioxide gas-sensitive material has a sensitivity of 34 for detecting 5 ppm hydrogen sulfide at 200 °C.[21] In 2016, Shi *et al.* studied reduced graphene oxide/hexagonal WO_3 nanosheet composites with a sensitivity of 45 for detecting 10 ppm hydrogen sulfide at 330 °C.[22] In 2017, Yang *et al.* reported a NiO cube (hc-NiO)/nitrogen doped reduced graphene oxide (N-rGO) composite with a sensitivity of 54.06 for 100 ppm hydrogen sulfide at 92 °C.[23] In 2018, Chu *et al.* reported that tin oxide-modified reduced graphene oxide (SnO_2–rGO) had a response value of 34.31 to 100 ppm hydrogen sulfide at 125 °C.[24] Modified graphene exhibits good performance for hydrogen sulfide, but the optimal operating temperature is still high, so gas-sensitive materials based on lower operating temperatures need further research.

As we all know, metal phthalocyanine is considered as an excellent organic thin film gas sensor because of its unique conjugated 18 π electronic structure, the diversity of the central atoms and the fact that the hydrogen atoms around the external phthalocyanine ring can be replaced by other groups to form a variety of phthalocyanine compounds. Many studies have shown that metal phthalocyanine can work at room temperature, and has good selectivity, high sensitivity and short response time. Different kinds of inorganic gases (SO_2, CO, CO_2) have been detected by adjusting the substituents, and volatile organic compounds were detected by using metal phthalocyanines with different central atoms.[25,26] However, single metal phthalocyanine gas sensors have a large resistance, and the original metal phthalocyanine gas sensor has fewer exposed active sites and a small contact area, which greatly limits its research in the field of gas sensing, so it has to be modified and assembled to enhance its gas sensing performance.

Based on the above research and discussion, in this paper, we use non covalent modification to prepare tetra-α-(4-trifluoromethylphenoxy)phthalocyanine cobalt/reduced graphene oxide (3-cF_3poPcCo/rGO) and tetra-β-(4-trifluoromethylphenoxy)phthalocyanine cobalt/reduced graphene oxide (4-cF_3poPcCo/rGO) hybrids. The strong π–π stacking between the reduced graphene oxide surface and the large π conjugated system of the phthalocyanine ring plane was used to induce the adsorption and assembly of phthalocyanine molecules on the graphene surface, so as to realize the improvement of the gas sensitivity of metal phthalocyanine and reduced graphene oxide. The effects of different substituent positions of the phthalocyanines on the gas sensing properties of the cF_3-poPcCo/rGO hybrid materials were studied. Due to the nonplanar distortion of the 3-cF_3poPcCo phthalocyanine complex, the (3-cF_3poPcCo/rGO) hybrid easily exhibits nonplanar distortion. Therefore, this study shows that the 4-cF_3poPcCo/rGO hybrid has more excellent gas sensing performance than the 3-cF_3poPcCo/rGO hybrid. Studies have shown that the sensitivity of 4-cF_3poPcCo/rGO to 1 ppm H_2S is as high as 46.58, and the minimum detection limit is 11.6 ppb at room temperature. In addition, the selectivity, reproducibility, stability, and gas sensing mechanism of hydrogen sulfide are discussed in detail (Scheme 1).

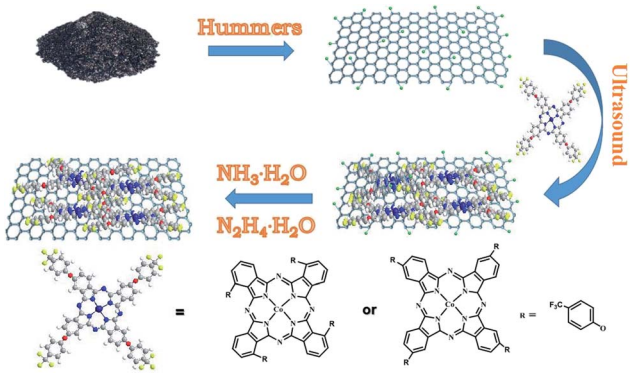

Scheme 1 Schematic diagram of the cF_3poPcCo/rGO hybrid synthesis procedure.

2. Experimental and calculation details

2.1 Materials and reagents

Flake graphite was purchased from Shenzhen Nanotech Port Co. Ltd. 3-Nitrophthalonitrile and 4-nitrophthalonitrile (99% purity), and DBU (98% purity) were purchased from Sigma-Aldrich Co. LLC. *p*-Trifluoromethylphenol (99% purity) was purchased from Shanghai SAEN Chemical Technology Co., Ltd. Ultrapure water (resistivity 18.2 MΩ cm) was obtained from a Milli-Q Water System (Millipore Corp., Bedford, MA, USA) and was used throughout the experiments. Graphene oxide (GO) was fabricated using the modified Hummers method from graphite powder, as described in our former reports.[27] Trifluoromethylphenoxyphthalocyanine cobalt (cF_3poPcCo) was synthesized by using the reaction of trifluoromethylphenoxyphthalonitrile with anhydrous cobalt chloride(II) in the presence of 1,8-diazabicyclo[5,4,0]undec-7-ene (DBU) (see Experiment details in the ESI†). All other reagents were of analytical grade and utilized without further purification.

2.2 Preparation of cF_3poPcCo/rGO hybrids

The cF_3poPcCo/rGO hybrids were prepared by using the same general methods; GO (0.100 g) was dispersed in 30 ml of *N*,*N*-dimethylformamide (DMF) solution, and ultrasonication was performed at room temperature for 2 h. cF_3poPcCo (0.200 g) dissolved in DMF solution (10 ml) was added to the dispersed GO solution dropwise. The subsequent mixture was ultrasonically treated at room temperature for 48 hours. Then, hydrazine hydrate (0.6 ml) and ammonia water (4 ml) were added and the mixture was stirred in a nitrogen atmosphere at 90–100 °C for 24 hours. After cooling, the solution was filtered through a 0.45 μm microporous filter, and washed with DMF, ethanol and acetone in turn until the filtrate was colorless. Then, the product was dried under vacuum at 50 °C for 5 h.

2.3 Fabrication and measurement of gas sensors

A full description of the gold electrodes and the gas sensor testing device is available in our previous research.[27,28]

In order to prepare the cF$_3$poPcCo/rGO hybrid gas sensor, the prepared cF$_3$poPcCo/rGO (1 mg) hybrid was dispersed in ethanol (1 ml) to obtain a uniform suspension of 1.0 mg ml^{-1}. After ultrasonic treatment for 3 hours, the dispersed solution was dropped onto an interdigital electrode with a micro syringe. After the solvent was completely evaporated, the sensor device was dried in a vacuum oven at 80 °C for 2.5 hours to completely remove the solvent residue. For comparison, a similar process was used to prepare the rGO and cF$_3$poPcCo gas sensors.

A typical sensor test cycle consists of three steps to speed up the recovery of the sensor. First, the testing chamber was cleaned by continuously blowing clean air, and then was evacuated using a pump. After that, the target gas was injected into a vacuum glass chamber *via* a microsyringe, and then fresh air (45 ± 5 RH%) was passed into the chamber to balance the inside and outside pressure of the chamber. The sensor was inserted into the chamber to get the gas response, and removed from the chamber to obtain the gas recovery. To avoid the effect of residual H_2S on the gas response, the gas sensing measurement was carried out in the order of low to high H_2S concentration. Besides, ppb levels of H_2S can be obtained by injecting various volumes of 1 ppm standard H_2S gas. All measurements were performed at 25 °C ± 1.0 °C with a relative humidity of 45% ± 5%. In this work, response is defined as the relative resistance change, as follows:

$$\text{Response} = \frac{\Delta R}{R} \times 100\% = \frac{R_g - R_0}{R_0} \times 100\% \quad (1)$$

where R_0 is the sensor resistance in the initial air flow, which was used as the background, and R_g is the sensor resistance after being exposed to a certain concentration of the target gas. The response and recovery times are defined as the time needed for 90% of the total resistance change on exposure to the target gas and air, respectively. The effect of the relative humidity on the gas response was evaluated with water vapors of various saturated salt solutions including KNO_3 (92%), NaCl (73%), K_2CO_3 (45%), $MgCl_2$ (33%) and LiCl (11%). The response toward different humidities is the ratio of the sensor resistance in air (R_a) under the test conditions (the relative humidity was 45 ± 5 RH%) to that in humid air (R_h).

2.4 Characterization

UV-vis absorption spectra were recorded with a UV-2700 UV-vis spectrometer (SHIMADZU, Japan). FT-IR spectra were recorded on a Spectra two FT-IR spectrometer (PerkinElmer, USA). The gaseous products after the cF$_3$poPcCo/rGO hybrid sensor contacted H_2S were investigated by gas chromatography/mass spectrometry (GC-MS, Thermo Scientific TRACE 1300). The scanning electron microscopy (SEM) images were recorded with a Hitachi S-4800 field emission scanning electron microscope operating at 15 kV. Thermogravimetric (TG) analysis was performed on a TA Q600 under a stream of nitrogen at a heating rate of 10 °C min^{-1}. Electrochemical impedance spectroscopy (EIS) was performed on a CHI760E electrochemical workstation at room temperature with a frequency range of 0.01 Hz to 100 kHz and an excitation amplitude of 0.2 V. The current voltage (*I–V*) characteristics of the sensor were measured by measuring the potential between −1 and +1 V at a scanning rate of 0.01 V s^{-1} on a Keithley 4200 semiconductor parameter analyzer.

3. Results and discussion

3.1 Characterization of the PcCo/rGO hybrids

In this study, 3(4)-(4-trifluoromethylphenoxy)phthalonitrile and 3(4)-cF$_3$poPcCo were synthesized. The GC-MS spectra of 3(4)-(4-trifluoromethylphenoxy)phthalonitrile are shown in Fig. S1 and S2,† which indicate that the rule of the molecular ion peaks is consistent with the structure of the molecular fragments. In order to confirm the preparation of cF$_3$poPcCo, the FT-IR characterization of these compounds is shown in Fig. 1A and S3A.† The vibration peak of O–H of 4-(trifluoromethyl)phenol disappeared at 3377 cm^{-1}, indicating the successful preparation of 4-(4-trifluoromethylphenoxy)phthalonitrile. Compared with 4-(4-trifluoromethylphenoxy)phthalonitrile, the C–N stretching vibration peak at 2243 cm^{-1} in 4-cF$_3$poPcCo disappeared, which confirmed that 4-(4-trifluoromethylphenoxy)phthalonitrile had been cyclized to form 4-cF$_3$poPcCo. The absorption peaks of 4-cF$_3$poPcCo and 4-(4-trifluoromethylphenoxy)phthalonitrile at 1330 cm^{-1} indicated that the characteristic vibration absorption peaks of C–F of 4-trifluoromethylphenol were retained, which also confirmed the successful preparation of 4-cF$_3$poPcCo and 4-(4-trifluoromethylphenoxy)phthalonitrile. Similarly, 3-cF$_3$poPcCo and 3-(4-trifluoromethylphenoxy)phthalonitrile are the same as 4-cF$_3$poPcCo and 4-(4-trifluoromethylphenoxy)phthalonitrile in Fig. S3A,† which shows that the metal phthalocyanine is formed by the cyclization of phthalonitrile, which also shows that the test results are consistent with the predicted structure.

Through the above discussion, we have successfully prepared metal cobalt phthalocyanine complexes. The infrared

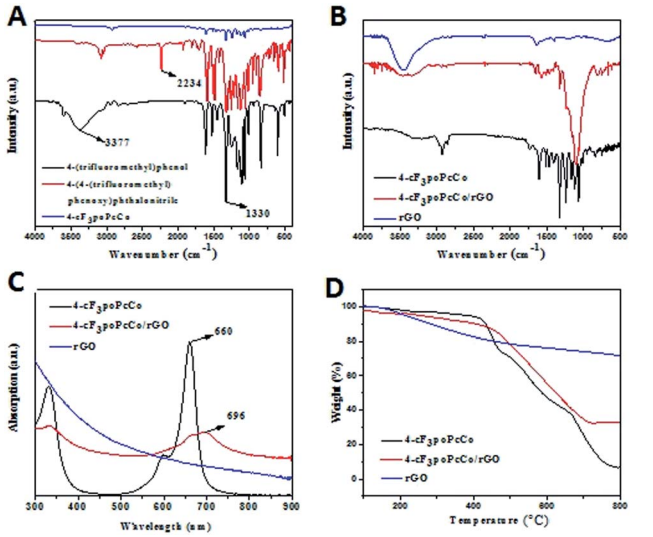

Fig. 1 (A) FT-IR spectra of 4-(trifluoromethyl)phenol, 4-(4-trifluoromethylphenoxy)phthalonitrile and the 4-cF$_3$poPcCo complex; (B) FT-IR spectra of rGO, 4-cF$_3$poPcCo and the 4-cF$_3$poPcCo/rGO hybrid; (C) UV-vis spectra of rGO, 4-cF$_3$poPcCo and the 4-cF$_3$poPcCo/rGO hybrid in DMF; (D) TG profiles of rGO, 4-cF$_3$poPcCo and the 4-cF$_3$poPcCo/rGO hybrid.

spectrum of the 4-cF$_3$poPcCo/rGO hybrid is shown in Fig. 1B. There are strong absorption peaks at 1636 and 3440 cm^{-1} of rGO, which correspond to the vibration peaks of C̄C and O–H of rGO, respectively, but no obvious absorption peaks are found at other positions, which proves that a large number of hydroxyl and carboxyl groups are lost in the formation of rGO after reduction, which also proves the successful preparation of rGO.[29] The vibration peaks of C̄C and O–H at 1636 and 3440 cm^{-1} were retained in the 4-cF$_3$poPcCo/rGO hybrid, and the characteristic absorption peaks of the 4-cF$_3$poPcCo hybrid were also observed in the wavelength range of 900–1600 cm^{-1}. For example, at about 1330 cm^{-1} is the stretching vibration peak of C–F, and at 1250 and 1086 cm^{-1} are the corresponding vibration peaks of aryl ether.[30,31] Similarly, for the 3-cF$_3$poPcCo/rGO hybrids, the C̄C and O–H peaks of rGO can also be clearly seen at 1636 and 3440 cm^{-1}, and the characteristic absorption peaks of the 3-cF$_3$poPcCo/rGO hybrid can be seen within the wavelength range of 900–1600 cm^{-1} in Fig. S3B.† In conclusion, all of these results confirm that the cF$_3$poPcCo complex has successfully adsorbed onto the surface of rGO in a noncovalent manner.

In order to further determine the prepared hybrids, we tested the UV-vis spectra of the rGO, 4-cF$_3$poPcCo and 4-cF$_3$poPcCo/rGO hybrids in DMF solution, as shown in Fig. 1C. The UV-vis spectrum of rGO in DMF solution exhibits no absorption peaks, which may be due to the poor dispersion of rGO in the DMF solution. Unlike rGO, the 4-cF$_3$poPcCo hybrid has a strong absorption peak at the Q band (660 nm), which is mainly attributed to the π–π* transition of the phthalocyanine ring from the HOMO (highest occupied molecular orbital) to the LUMO (lowest unoccupied molecular orbital). A small absorption peak appears at about 600 nm, which is mainly caused by n–π* transition. In addition, there are other peaks between 300–400 nm in the B-band region (UV region) because of the deeper π–π* transition, but the intensity is low. In general, the Q-band absorption of the substituted metal phthalocyanine is red-shifted compared with that of the unsubstituted metal phthalocyanine, because the HOMO–LUMO energy gap of the phthalocyanine ring is reduced by the introduction of substituents.[32] If there are different halogen atoms (bromine, fluorine and chlorine) in the phthalocyanine ring, these bands will blue-shift relative to the corresponding non-fluorinated metal phthalocyanine due to the electron absorption properties of the halogen atoms. Therefore, the 4-cF$_3$poPcCo is blue-shifted by 4 nm compared with poPcCo.[33] The blue-shift of 4-cF$_3$poPcCo was also observed compared with the 3-cF$_3$poPcCo complex (Fig. S3C†). These shifts might be due to the non-planar distortion of the non-peripheral substituted metallophthalocyanine (3-cF$_3$poPcCo) being easier than for the peripheral substituted metallophthalocyanine (4-cF$_3$poPcCo). The HOMO level is more unstable at the non-peripheral position and the energy gap between the HOMO–LUMO levels becomes smaller, resulting in a red-shift.[34] This result indicates that the position of the substituent group in 4-cF$_3$poPcCo reduces the molecular non-planarity, decreases the conjugation of the macrocycle and hence shifts the absorption maximum wavelength hypsochromically. Therefore, the 4-cF$_3$poPcCo/rGO hybrid may show better gas sensing performance than the 3-cF$_3$poPcCo/rGO hybrid due to the use of peripheral substitution by 4-trifluoromethylphenoxy groups and adjustment of the substituent position. This is in line with the gas sensing performance of the phthalocyanine compounds bearing tetra-(3,6-dihexyl-7-oxy-4-methylcou-marin) units.[34]

Compared with that of the 4-cF$_3$poPcCo hybrid, the UV-vis spectrum of the 4-cF$_3$poPcCo/rGO hybrid shows a broadened Q-band and a red-shift of 36 nm, which indicates that charge is transferred from the cF$_3$poPcCo hybrid to rGO, and that the cF$_3$poPcCo hybrid has been successfully adsorbed onto the surface of rGO.[35] Similarly, in the UV-vis spectrum of the 3-cF$_3$poPcCo/rGO hybrid (Fig. S3C†), the peak of the 3-cF$_3$poPcCo complex is broadened and a red-shift of 28 nm is observed. On the other hand, the bands of 4-cF$_3$poPcCo/rGO are noticeably broadened and red-shifted as compared with 3-cF$_3$poPcCo/rGO. This result indicates that 4-cF$_3$poPcCo/rGO shows a bigger charge transfer interaction from 4-cF$_3$poPcCo to rGO, which will also benefit the gas sensitivity of the 4-cF$_3$poPcCo/rGO hybrid.

In order to verify the content of phthalocyanine adsorbed on the rGO by the cF$_3$poPcCo complex, the TG of rGO, cF$_3$poPcCo and cF$_3$poPcCo/rGO was studied in a N_2 atmosphere, as shown in Fig. 1D and S3D.† The weight loss of rGO is about 17.22% in the range of 300–600 °C, which is mainly due to the destruction of oxidized species and residual amorphous carbon on the surface of rGO, as shown in Fig. 1D and S3D.† The weight loss of 4-cF$_3$poPcCo is 56.13% in the same temperature range, which is mainly due to the destruction of the phthalocyanine peripheral substituent group. The weight loss of 4-cF$_3$poPcCo/rGO is 30.75%, originating from the above-mentioned destruction of the phthalocyanine and rGO. Thus, a corrected weight loss of 13.53% (30.75–17.22%) can be obtained, which comes from 4-cF$_3$poPcCo in the 4-cF$_3$poPcCo/rGO hybrid. Considering the actual amount of 4-cF$_3$poPcCo adsorbed on the surface of rGO, a real ratio of 24.10% (13.53%/56.13%) can be calculated. The content of 3-cF$_3$poPcCo in the 3-cF$_3$poPcCo/rGO hybrid was 11.95% by the same method. This result shows that the amount of phthalocyanine in the 4-cF$_3$poPcCo/rGO hybrid is higher than that of the 3-cF$_3$poPcCo/rGO hybrid, and indicates that the non-planar distortion of 3-cF$_3$poPcCo has a negative effect on the preparation of hybrids. Therefore, the 4-cF$_3$poPcCo/rGO hybrid may exhibit superior gas sensitivity compared to the 3-cF$_3$poPcCo/rGO hybrid.

3.2 Gas sensing properties

The SEM image of the 4-cF$_3$poPcCo/rGO hybrid on an interdigital electrode is shown in Fig. 2A–C. Compared with the 3-cF$_3$poPcCo/rGO hybrid (Fig. 2D–F), the scanning electron microscope layer of the 4-cF$_3$poPcCo/rGO hybrid is clearer, and it is distributed evenly and loosely between the two fingers of the interdigital electrode, which provides a continuous conductive path for electron transmission, a permeable channel for gas molecular diffusion, and more advantages at the active site. Moreover, the structure of reduced graphene oxide can be clearly seen on the interdigital electrode substrate. This porous surface morphology is conducive to the adsorption and

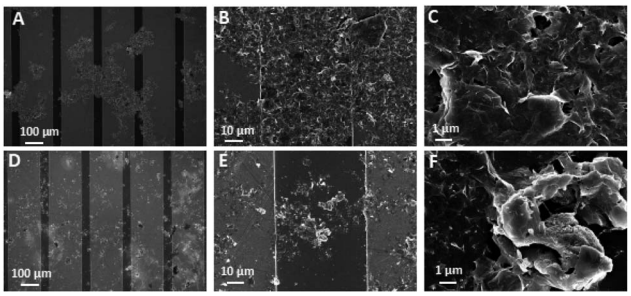

Fig. 2 SEM images of the (A–C) 4-cF$_3$poPcCo/rGO and (D–F) 3-cF$_3$poPcCo/rGO hybrids on an interdigital electrode.

desorption of gas molecules, which will improve the sensing performance of the hybrid.

Through the observation of the 3-cF$_3$poPcCo/rGO hybrid and the 4-cF$_3$poPcCo/rGO hybrid (Fig. 2 and S4†), the microstructure of the 4-cF$_3$poPcCo/rGO hybrid clearly exhibits a uniform lamellar structure with many gaps between the layers. However, the stacking phenomenon of the 3-cF$_3$poPcCo/rGO hybrid also shows that the 3-cF$_3$poPcCo with non-planarity cannot easily form a non-covalent hybrid with reduced graphene oxide, which will lead to the stacking phenomenon. The formation of this stacking phenomenon may lead to the difference in gas sensitivity between the two hybrids. Finally, the accuracy of this interpretation is confirmed by studying the sensitivity of the 4-cF$_3$poPcCo/rGO hybrid and 3-cF$_3$poPcCo/rGO hybrid to hydrogen sulfide gas.

Selectivity is a very important characteristic in the application of sensors at room temperature. The gas sensing characteristics of cF$_3$poPcCo, rGO and the cF$_3$poPcCo/rGO hybrid sensors deposited on interdigital electrodes were studied using hydrogen sulfide as the target gas. The responses of the five sensors to 1 ppm H_2S and 1000 ppm of 15 different other gases have been studied, and the results are shown in Fig. 3A. The sensors based on the cF$_3$poPcCo/rGO hybrids show the highest response to H_2S; in particular, the response value of 4-cF$_3$-poPcCo/rGO for 1 ppm H_2S is as high as 46.58%. Compared with other gases, the 4-cF$_3$poPcCo/rGO hybrid exhibits excellent selectivity to H_2S. For the other sensors, the sensitivity of phthalocyanine is not high enough, although its selectivity to H_2S is high. However, the response and selectivity of the rGO sensor to H_2S are poor, so we chose hydrogen sulfide as the research object of gas detection and carried out a series of tests. The influence of humidity on the sensor is also an important factor in the application of the sensor at room temperature. Therefore, the response of the cF$_3$poPcCo/rGO hybrid sensor to 1 ppm H_2S was tested under different relative humidities at 25 °C. As shown in Fig. 3B, under different relative humidities, the response of the cF$_3$poPcCo/rGO hybrid sensor to 1 ppm H_2S hardly changed, which indicates that the prepared material has strong stability in the ambient environment. Based on the above results, the cF$_3$poPcCo/rGO hybrid sensor shows higher selectivity and lower RH effect in terms of sensing response. Therefore, cF$_3$poPcCo/rGO hybrid materials are expected to be used as H_2S sensing materials.

In order to further study the gas sensing characteristics of cF$_3$poPcCo/rGO towards H_2S, the dynamic response recovery curve of the 4-cF$_3$poPcCo/rGO hybrid to H_2S at different concentrations was recorded as shown in Fig. 4A. The signal resistance is continuously recorded because the sensor sample is exposed to the target gas in a gas tight chamber and then recovers at room temperature. For comparison, the sensing response of 4-cF$_3$poPcCo and rGO to H_2S was also studied. Nine dynamic cycles corresponding to 0.1–40 ppm H_2S concentration were recorded continuously at room temperature. It can be seen that with the increase of the H_2S concentration, the response strength of all of the sensors will increase. In addition, the response of the 4-cF$_3$poPcCo/rGO sensor to the H_2S concentration shows two good linear responses as shown in Fig. 4B. The concentration in the range of 0.1–1 ppm is 4.56% H_2S per ppm, and the concentration in the range of 1–20 ppm is 0.27% H_2S per ppm. The linear regression equation $S = 4.56C$ (ppm) + 41.99 ($R^2 = 0.999$) is obtained from the calibration curve, which shows that the detection limit (LOD) of the 4-cF$_3$poPcCo/rGO

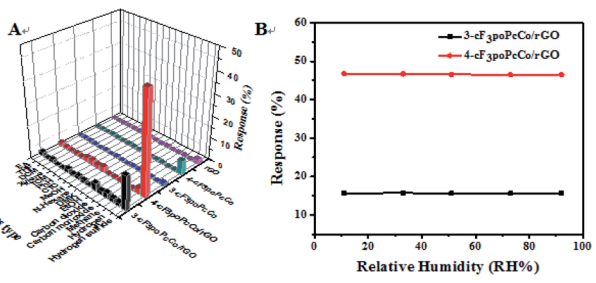

Fig. 3 (A) Response of RPcCos, rGO and RPcCo/rGO hybrid-based sensors to 1 ppm of H_2S and 1000 ppm of various other gases, respectively. (B) Response of the cF$_3$poPcCo/rGO hybrid-based sensors to 1 ppm H_2S at different relative humidities at 25 °C.

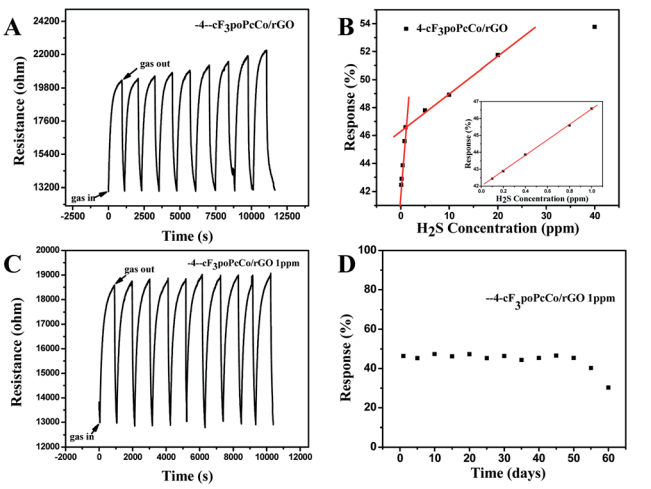

Fig. 4 (A) Resistance of the 4-cF$_3$poPcCo/rGO hybrid sensor upon exposure to varying concentrations of H_2S; (B) relationship of the response of the 4-cF$_3$poPcCo/rGO hybrid sensor to the concentration H_2S; (C) ten sensing cycles of the 4-cF$_3$poPcCo/rGO hybrid sensor to 1 ppm H_2S; (D) the reproducibility characteristics of the 4-cF$_3$poPcCo/rGO hybrid sensor to 1 ppm H_2S within 60 days at 25 °C.

sensor is as low as 11.6 ppb (S/N = 3) according to the reported method. The points were averaged and a standard deviation (S) was gathered as 0.25. Therefore, the sensor noise is 0.0177 according to eqn (2) and the theoretical detection limit (for a signal-to-noise ratio of 3) is approximately 11.6 ppb according to eqn (3).[36,37]

$$\mathrm{RMS_{noise}} = \sqrt{\frac{S^2}{N}} = 0.0177 \quad (2)$$

$$\mathrm{LOD\ (ppm)} = 3 \times \frac{\mathrm{RMS_{noise}}}{\mathrm{slope}} = 11.6\ \mathrm{ppb} \quad (3)$$

Repeatability and stability are also important factors in the evaluation of gas sensors. The cycling stability and long-term stability of 1 ppm H_2S were measured at room temperature. After 10 cycles, the 4-cF$_3$poPcCo/rGO sensor still maintains rapid response and recovery capability, and the response is almost the same, as shown in Fig. 4C. In addition, the response changes only about 5.0% after 50 days (Fig. 4D), which also shows that the 4-cF$_3$poPcCo/rGO sensor has excellent long-term stability for H_2S.

The H_2S sensing performance of the 3-cF$_3$poPcCo/rGO sensor is shown in Fig. S5.† It also shows high sensitivity, good linear response, long-term stability and repeatability, as well as lower detection concentration. However, the sensitivity of the 4-cF$_3$poPcCo/rGO hybrid was higher than that of the 3-cF$_3$poPcCo/rGO hybrid. As mentioned above in the UV-vis and TG spectra, the peripheral substituted group of the 4-cF$_3$poPcCo complex tends to form a planar structure, and has a positive effect on the preparation of hybrids and the evenly distributed, loose and porous surface morphology of the sensor. Therefore, the 4-cF$_3$poPcCo/rGO hybrid shows better gas sensing performance than the 3-cF$_3$poPcCo/rGO hybrid. As shown in Fig. S6A,† the sensitivity of 4-cF$_3$poPcCo/rGO, 3-cF$_3$poPcCo/rGO, 4-cF$_3$poPcCo, 3-cF$_3$poPcCo and rGO sensors at several different H_2S concentrations was studied. For example, the sensitivity of the 4-cF$_3$poPcCo/rGO hybrid is about 2.98 times, 18.85 times, 41.58 times and 36.67 times higher than that of the 3-cF$_3$poPcCo/rGO, 4-cF$_3$poPcCo, 3-cF$_3$poPcCo and rGO sensors for 1 ppm H_2S, respectively. In particular, 4-cF$_3$poPcCo/rGO also exhibits much higher sensitivity, lower detection limits and optimal operating temperatures compared to previously reported gas-sensitive materials (Table S1†). This is mainly because the introduced trifluoromethyl group will reduce the electron cloud density and increase the holes on the phthalocyanine, which will facilitate the adsorption of gas molecules and increase its gas sensitivity.

In order to further explore the effect of substituents on the gas sensing performance, the gas sensing properties of the tetra-β-(phenoxy)cobalt phthalocyanine and graphene oxide (4-poPcCo/rGO) and tetra-β-(carboxyphenoxy)cobalt phthalocyanine and graphene oxide (4-cpoPcCo/rGO) hybrids were tested. The research shows that the sensitivity to 1 ppm H_2S of 4-cF$_3$poPcCo/rGO is 9.1 times and 19.2 times higher than that of 4-cpoPcCo/rGO and 4-poPcCo/rGO, as shown in Fig. S6B,† thus successfully confirming that the substituent has a great influence on the sensitivity of the gas sensor. When the electron-withdrawing group is outside the phthalocyanine ring, it reduces the electron cloud density of the phthalocyanine ring and increases the holes on the phthalocyanine ring. Therefore, when the reductive gas H_2S contacts with it, the lone pair electrons of the gas molecules will be more easily transferred to the phthalocyanine, which is conducive to increasing the resistance of the hybrid materials and the sensitivity of the gas sensor. Therefore, the corresponding gas sensing performance will also decrease in turn because the electronegativity of trifluoromethylphenoxy, carboxyphenoxy and phenoxy decreases in turn.

3.3 Gas sensitivity mechanism

The sensing mechanism of phthalocyanine and graphite oxide for hydrogen sulfide is in accordance with charge transfer theory, as shown in Scheme 2. Therefore, the adsorption of the target gas on the surface of the H_2S gas sensor changes its resistance, which is very similar to the principle of the sensing mechanism in metal oxide gas sensors.[38] In air, oxygen molecules have high electron affinity (0.43 eV (ref. [39])) and can easily adsorb on the surface of the cF$_3$poPcCo/rGO hybrid. After that, the oxygen molecules capture the free electrons from the cF$_3$poPcCo/rGO hybrids and generate chemically adsorbed oxygen substances in the form of O_2^- (eqn (4) and (5), $T < 100$ °C).[40–43] This leads to an increase in the concentration of hole carriers. When exposed to H_2S, the H_2S gas will interact with the adsorbed oxygen O_2^- (eqn (6) and (7)).[35,42] Meanwhile, a large number of electrons will be released.[35] The electrons generated are trapped by the cF$_3$poPcCo/rGO hybrids through the phthalocyanine absorbed on the surface of rGO. Electrons recombine with holes and decrease the density of the hole carriers in the process of sensing, which leads to an increase in resistance, as shown in Scheme 2. In order to verify the interaction between the cF$_3$poPcCo/rGO sensor and H_2S, after the 4-cF$_3$poPcCo/rGO hybrid was exposed to H_2S for 1 h, the gaseous product was measured by GC-MS. The results in Fig. 5 show that the molecular ion of SO_2 ($m/z = 64$) appeared. These results indicate that H_2S is oxidized to SO_2, in accordance with the above sensing mechanism.[35]

$$O_2(g) \rightarrow O_2(ads) \quad (4)$$

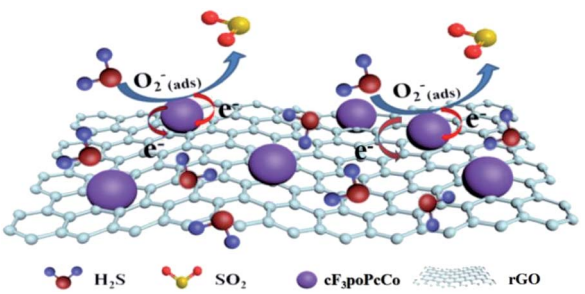

Scheme 2 Schematic diagram of the gas sensing mechanism *via* the interaction between the cF$_3$poPcCo/rGO sensor and H_2S.

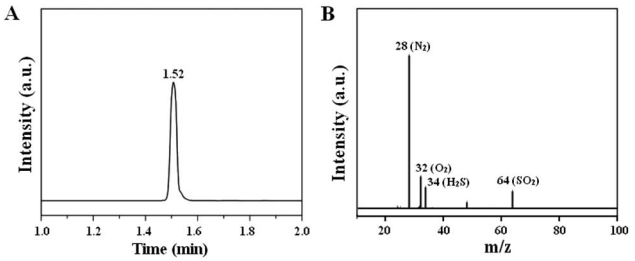

Fig. 5 (A) Gas chromatogram and (B) mass spectrum after 4-cF$_3$-poPcCo/rGO sensor exposure to H_2S at 25 °C.

$$O_2(ads) + e^- \rightarrow O_2^-(ads) \quad (5)$$

$$H_2S(g) \rightarrow H_2S(ads) \quad (6)$$

$$2H_2S(ads) + 3O_2^-(ads) \rightarrow 2H_2O(g) + 2SO_2(g) + 3e^- \quad (7)$$

Why the cF$_3$poPcCo/rGO hybrids display excellent H_2S-sensing performance can be explained as follows: first, the loose and porous structure enables gas molecules to adsorb and transfer rapidly throughout the sensing layer, and provides more active sites and channels for the reaction between H_2S gas and the adsorbed oxygen O_2^-. Second, the graphene is an excellent conductive agent. Adding an appropriate amount of graphene can quickly capture the generated electrons coming from eqn (7), leading to a fast and sensitive response. Finally, the electron-withdrawing capability of the trifluoromethyl group can increase the holes of rGO and PcCo. These holes quickly capture the generated electrons in the gas sensing process, which can reduce the carrier concentration of the cF$_3$poPcCo/rGO hybrid and the resistance of the cF$_3$poPcCo/rGO sensor is increased. In this system, the electron-withdrawing capability of the trifluoromethyl group has a great influence on the H_2S-sensing performance.

In order to verify the H_2S sensing mechanism, the *I–V* characteristic curve of the sensing device is shown in Fig. 6 and S7.† The linearity and symmetry of the *I–V* curve indicate the ohmic contact between the sample and the gold electrode. Obviously, under the same voltage, the current of all kinds of sensing devices decreases gradually according to the law of rGO > 4-cF$_3$poPcCo/rGO > 4-cF$_3$poPcCo/rGO exposed to H_2S > 4-cF$_3$poPcCo, and 4-cF$_3$poPcCo/rGO > 3-cF$_3$poPcCo/rGO. Low current means that the sensor has a relatively high resistance. The cF$_3$poPcCos show high resistance due to their inherently high resistance. For the cF$_3$poPcCo/rGO hybrids, it may be due to the inherently high resistance of cF$_3$poPcCo and the donation of electrons from p-type cF$_3$poPcCo to p-type rGO to reduce the current of the device compared with rGO. The distinct difference in device current of the two cF$_3$poPcCo/rGO hybrids is ascribed to the different position of the substituents. Non-peripheral substituents have stronger electron-donating capability than peripheral substituents.[34] This can provide more electron binding on the holes of p-type semiconductor 3-cF$_3$-poPcCo and rGO. The combination of electrons and holes can

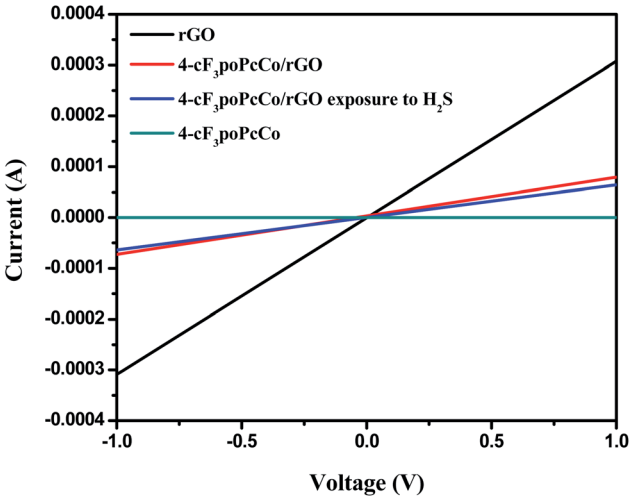

Fig. 6 *I–V* curves of the rGO, 4-cF$_3$poPcCo, 4-cF$_3$poPcCo/rGO and 4-cF$_3$poPcCo/rGO exposed to H_2S.

reduce the carrier concentration of the system, which will further increase the resistance of the 3-cF$_3$poPcCo/rGO hybrid. This is very consistent with the analysis results of the band gap from the UV-visible diffuse reflectance spectra (Fig. S8†). Hence, the response towards H_2S is not as good as that of the 4-cF$_3$-poPcCo/rGO hybrid. When the cF$_3$poPcCo/rGO hybrids contact H_2S, the resistance of the cF$_3$poPcCo/rGO hybrids is further increased due to the fact that H_2S is used as an electron donor with a pair of lone electrons. This is very consistent with the charge transfer mechanism.

In order to further evaluate the conductivity of cF$_3$poPcCos, the HOMO–LUMO energy levels of 3-cF$_3$poPcCo and 4-cF$_3$-poPcCo were calculated using density functional theory (DFT) with the spin-polarized gradient corrected functional of Perdew, Burke, and Ernzerhof (PBE) as implemented in the VASP package.[44,45] The projector augmented wave (PAW) method with a planewave basis set was employed.[46] The *Γ*-point approximation was employed for Brillouin zone integration. Charge analyses were performed with Bader analysis. The calculation results show that the HOMO–LUMO energy level of 4-cF$_3$poPcCo (1.12 eV) is slightly smaller than that of 3-cF$_3$poPcCo (1.13 eV), which indicates that 4-cF$_3$poPcCo/rGO has higher conductivity compared to 3-cF$_3$poPcCo/rGO. Moreover, the valence and conduction bands of phthalocyanine correspond to the HOMO and LUMO of phthalocyanine molecules, respectively.[47] In order to further determine the band gap of cF$_3$poPcCos, UV-visible diffuse reflectance spectra of cF$_3$poPcCos were measured. Fig. S8b–e† show the optical absorption spectra of cF$_3$poPcCos, from which the band gaps of 3-cF$_3$poPcCo and 4-cF$_3$poPcCo can be estimated from the plot of $(Ahv)^2$ (for direct band gap) *versus* photon energy (hv). The intercepts of the tangent to the *x*-axis give a good approximation of the band gap of 3-cF$_3$poPcCo and 4-cF$_3$poPcCo to be approximately 1.38 and 1.28 eV, respectively. Which further indicates that the conductivity of 4-cF$_3$poPcCo is higher than that of 3-cF$_3$poPcCo. Hence, the response of 3-cF$_3$poPcCo/rGO towards H_2S is not as good as that of the 4-cF$_3$poPcCo/rGO hybrid.

Table 1 Fitted impedance parameters of rGO, cF3poPcCo and cF3poPcCo/rGO electrode

Samples	R_b (Ω)	R_{ct} (Ω)
4-cF_3poPcCo/rGO	11.05	9.56
3-cF_3poPcCo/rGO	16.32	27.57
3-cF_3poPcCo	38.34	201.01
4-cF_3poPcCo	40.55	200.21
rGO	44.72	1887

In order to study the charge transfer kinetics of the hybrids, we measured the electrochemical impedance of rGO, cF_3-poPcCo and cF_3poPcCo/rGO, as shown in Fig. S8A.† The Nyquist diagram is installed through an appropriate electrical equivalent circuit, and the impedance diagram fitted by the equivalent circuit is shown in Fig. S8B.† It can be seen that the chemical impedance Nyquist diagram of the cF_3poPcCo/rGO hybrid after fitting shows a better relationship between the ground wire properties, as shown in Fig. S8C.† After fitting, the fitted electrode impedance parameters of rGO, cF_3poPcCo and the cF_3-poPcCo/rGO hybrid are also obtained, as shown in Table 1. R_b is the uncompensated resistance of the electrolyte, separator and electrode, and R_{ct} is the charge transfer resistance at the interface of the active material. It can be clearly seen that the R_b and R_{ct} of the 4-cF_3poPcCo/rGO hybrid are 11.05 Ω and 9.56 Ω, respectively, and are smaller than those of 3-cF_3poPcCo/rGO (16.32 Ω, 27.57 Ω), 3-cF_3poPcCo (38.34 Ω, 201.01 Ω), 4-cF_3-poPcCo (40.55 Ω, 200.21 Ω) and rGO (44.72 Ω, 1887 Ω). R_b and R_{ct} are related to the conductivity and electron transport of materials. The lower the R_b and R_{ct} values, the stronger the electron transport ability. This is in line with the results of electronic absorption spectra. Therefore, the 4-cF_3poPcCo/rGO hybrid shows better response to hydrogen sulfide than other sensing materials.

4. Conclusions

In conclusion, by designing and adjusting the peripheral substitution and substituent position of phthalocyanine, two kinds of cF_3poPcCo/rGO hybrids were successfully prepared and used for a high performance ppb-level hydrogen sulfide (H_2S) sensor at room temperature. The results show that the 4-cF_3poPcCo/rGO sensor exhibits improved gas sensing performance to H_2S due to the 4-trifluoromethylphenoxy group and peripheral substituent position of 4-cF_3poPcCo, including enhanced selectivity and response, and decreased recovery time for 1 ppm H_2S. In particular, the response sensitivity of the 4-cF_3poPcCo/rGO sensor to 1 ppm H_2S can be as high as 46.58%, with a fast recovery time of 50 s and a low detection limit of 11.6 ppb. Such excellent ppb-level H_2S gas sensing performance is mainly ascribed to the unique structure of the cF_3poPcCo/rGO hybrid. First, the loose and porous structure enables gas molecules to adsorb and transfer rapidly throughout the sensing layer, and provides more active sites and channels for the reaction between H_2S gas and the adsorbed oxygen O_2^-. Second, the graphene is an excellent conductive agent. Adding an appropriate amount of graphene can quickly capture the generated electrons coming from eqn (7), leading to a fast and sensitive response. Finally, the electron-withdrawing capability of the trifluoromethyl group can increase the holes of rGO and PcCo. These holes quickly capture the generated electrons in the gas sensing process, which can reduce the carrier concentration of the cF_3poPcCo/rGO hybrid and the resistance of the cF_3poPcCo/rGO sensor is increased. In this system, the electron-withdrawing capability of the trifluoromethyl group has a great influence on the H_2S-sensing performance. Therefore, the as-prepared cF_3poPcCo/rGO hybrids can be used as a practical candidate for ppb-level H_2S detection, and it is an effective way to design other functional gas sensing materials based on rGO by adjusting the peripheral substitution of phthalocyanine.

Conflicts of interest

There are no conflicts to declare.

Acknowledgements

We gratefully acknowledge financial support from the National Natural Science Foundation of China (51202061), the Natural Science Foundation of Heilongjiang Province of China (2019LH0320), and the Innovative Talents Program of Harbin (2017RAQXJ143).

References

1 H. B. Na, X. F. Zhang, M. Zhang, Z. P. Deng, X. L. Cheng, L. H. Huo and S. Gao, *Sens. Actuators, B*, 2019, **297**, 126816.
2 Z. L. Wu, Z. J. Li, H. Li, M. X. Sun, S. B. Han, C. Cai, W. Z. Shen and Y. Q. Fu, *ACS Appl. Mater. Interfaces*, 2019, **11**, 12761–12769.
3 Y. L. Tang, X. F. Xu, S. B. Han, C. Cai, H. R. Du, H. Zhu, X. T. Zu and Y. Q. Fu, *Sens. Actuators, B*, 2020, **304**, 127395.
4 R. K. Jha, J. V. D'Costa, N. Sakhuja and N. Bhat, *Sens. Actuators, B*, 2019, **297**, 126687.
5 Z. K. Xu, Y. Y. Luo and G. T. Duan, *ACS Appl. Mater. Interfaces*, 2019, **11**, 8164–8174.
6 X. N. Wu, S. S. Xiong, Y. Gong, Y. J. Gong, W. W. Wu, Z. H. Mao, Q. Liu, S. Hu and X. G. Long, *Sens. Actuators, B*, 2019, **292**, 32–39.
7 Y. J. Chen, F. N. Meng, H. L. Yu, C. L. Zhu, T. S. Wang, P. Gao and Q. Y. Ouyang, *Sens. Actuators, B*, 2013, **176**, 15–21.
8 Y. H. Li, W. Luo, N. Qin, J. P. Dong, J. Wei, W. Li, S. S. Feng, J. C. Chen, J. Q. Xu, A. A. Elzatahry, M. H. Es-Saheb, Y. H. Deng and D. Y. Zhao, *Angew. Chem., Int. Ed.*, 2014, **53**, 9035–9040.
9 J. Hu, G. L. Yin, J. C. Chen, M. Y. Ge, J. Lu, Z. Yang and D. N. He, *Phys. Chem. Chem. Phys.*, 2015, **17**, 20537–20542.
10 Z. S. Hosseini, A. Irajizad and A. Mortezaali, *Sens. Actuators, B*, 2015, **207**, 865–871.
11 Z. J. Li, Y. W. Huang, S. C. Zhang, W. M. Chen, Z. Kuang, D. Y. Ao, W. Liu and Y. Q. Fu, *J. Hazard. Mater.*, 2015, **300**, 167–174.

12 Z. J. Li, J. Q. Wang, N. N. Wang, S. N. Yan, W. Liu, Y. Q. Fu and Z. G. Wang, *J. Alloys Compd.*, 2017, **725**, 1136–1143.
13 Y. Chen, P. C. Xu, T. Xu, D. Zheng and X. X. Li, *Sens. Actuators, B*, 2017, **240**, 264–272.
14 X. X. Zhong, Y. B. Shen, S. K. Zhao, T. T. Li, R. Lu, Y. Y. Yin, C. Han, D. Z. Wei, Y. H. Zhang and K. F. Wei, *Vacuum*, 2019, **167**, 118–128.
15 D. J. Li, Y. L. Tang, D. Y. Ao, X. Xiang, S. Y. Wang and X. T. Zu, *Int. J. Hydrogen Energy*, 2019, **44**, 3985–3992.
16 H. B. Na, X. F. Zhang, Z. P. Deng, Y. M. Xu, L. H. Huo and S. Gao, *ACS Appl. Mater. Interfaces*, 2019, **11**, 11627–11635.
17 Y. C. Guo, X. Q. Tian, X. F. Wang and J. Sun, *Sens. Actuators, B*, 2019, **293**, 136–143.
18 Z. J. Lin, N. N. Wang, Y. W. Huang, J. Q. Wang, W. Liu, Y. Q. Fu and Z. G. Wang, *Mater. Des.*, 2016, **110**, 532–539.
19 H. Kheel, G. J. Sun, J. K. Lee, S. Lee, R. P. Dwivedi and C. Lee, *Ceram. Int.*, 2016, **42**, 18597–18604.
20 P. L. Quang, N. D. Cuong, T. T. Hoa, H. T. Long, C. M. Hung, D. T. T. Le and N. V. Hieu, *Sens. Actuators, B*, 2018, **270**, 158–166.
21 S. Choi, B. Jang, S. Lee, B. K. Min, A. Rothschild and I. Kim, *ACS Appl. Mater. Interfaces*, 2014, **6**, 2588–2597.
22 J. Shi, Z. Cheng, L. Gao, Y. Zhang, J. Xu and H. Zhao, *Sens. Actuators, B*, 2016, **230**, 736–745.
23 M. Yang, X. Zhang, X. Cheng, Y. Xu, S. Gao, H. Zhao and L. Huo, *ACS Appl. Mater. Interfaces*, 2017, **9**, 26293–26303.
24 J. Chu, X. Wang, D. Wang, A. Yang, P. Lv, Y. Wu, M. Rong and L. Gao, *Carbon*, 2018, **135**, 95–103.
25 S. Altun, E. B. Orman, Z. Odabas, A. Altindal and A. R. Ozkaya, *Dalton Trans.*, 2015, **44**, 4341–4354.
26 F. I. Bohrer, C. N. Colesniuc, J. Park, M. E. Ruidiaz, I. K. Schuller, A. C. Kummel and W. C. Trogler, *J. Am. Chem. Soc.*, 2009, **131**, 478–485.
27 X. Q. Zhou, X. L. Wang, B. Wang, Z. M. Chen, C. Y. He and Y. Q. Wu, *Sens. Actuators, B*, 2014, **193**, 340–348.
28 B. Wang, X. Q. Zhou, Y. Q. Wu, Z. M. Chen and C. Y. He, *Sens. Actuators, B*, 2012, **171**, 398–404.
29 P. Y. Zhu, M. Shen, S. H. Xiao and D. Zhang, *Phys. B*, 2011, **406**, 498–502.
30 T. Saka and N. Kahriman, *J. Organomet. Chem.*, 2019, **895**, 48–54.
31 A. K. Burat, Z. A. Bayır and A. Koca, *Electroanalysis*, 2014, **24**, 338–348.
32 R. Seoudi, G. S. El-Bahy and Z. A. El Sayed, *Opt. Mater.*, 2006, **29**, 304–312.
33 Z. J. Guo, B. Wang, X. L. Wang, Y. Li, S. J. Gai, Y. Q. Wu and X. L. Cheng, *RSC Adv.*, 2019, **9**, 37518–37525.
34 G. Ö. Artuç, A. Altındal, B. B. Eran and M. Bulut, *Dyes Pigm.*, 2019, **171**, 107741.
35 H. Wu, Z. M. Chen, J. L. Zhang, F. Wu, C. Y. He, B. Wang, Y. Q. Wu and Z. Y. Ren, *J. Mater. Chem. A*, 2016, **4**, 1096–1104.
36 M. Li, D. X. Zhou, J. Zhao, Z. P. Zheng, J. G. He, L. Hu, Z. Xia, J. Tang and H. Liu, *Sens. Actuators, B*, 2015, **217**, 198–201.
37 Z. L. Song, Z. R. Wei, B. C. Wang, Z. Luo, S. M. Xu, W. K. Zhang, H. X. Yu, M. Li, Z. Huang, J. F. Zang, F. Yi and H. Liu, *Chem. Mater.*, 2016, **28**, 1205–1212.
38 Y. J. Kwon, H. G. Na, S. Y. Kang, M. S. Choi, J. H. Bang, T. W. Kim, A. Mirzaei and H. W. Kim, *Sens. Actuators, B*, 2017, **239**, 180–192.
39 A. A. Manea, M. P. Suryawanshi, J. H. Kim and A. V. Moholkar, *J. Colloid Interface Sci.*, 2016, **483**, 220–231.
40 W. Chen, Y. Liu, Z. Qin, Y. Wu, S. Li and P. Ai, *Sensors*, 2015, **15**, 29950–29957.
41 R. Bari, P. Patil, S. Patil and A. Bari, *Bull. Mater. Sci.*, 2013, **36**, 967–972.
42 N. Barsan and U. Weimar, *J. Electroceram.*, 2001, **7**, 143–167.
43 N. S. Ramgir, P. K. Sharma, N. Datta, M. Kaur, A. K. Debnath, D. K. Aswal and S. K. Gupta, *Sens. Actuators, B*, 2013, **186**, 718–726.
44 G. Kresse and J. Hafner, *Phys. Rev. B: Condens. Matter Mater. Phys.*, 1993, **47**, 558–561.
45 G. Kresse and J. Furthmuller, *Phys. Rev. B: Condens. Matter Mater. Phys.*, 1996, **54**, 11169–11186.
46 P. E. Blöchl, Projector augmented-wave method, *Phys. Rev. B: Condens. Matter Mater. Phys.*, 1994, **50**, 17953–17979.
47 E. Condadell and S. Alvarez, *Inorg. Chem.*, 1984, **23**, 573–579.